





RESEARCH ARTICLE | MARCH 11 2025

Fluid propagation and protein adsorption patterns in porous nitrocellulose membranes for lateral flow assays

Alexander Spreinat ; Willfried Kunz ; Christian H. Maack; Carola Wilczek ; Britta Nestler ; Andrea Ernst



Physics of Fluids 37, 032022 (2025)

<https://doi.org/10.1063/5.0257343>



View
Online



Export
Citation

Articles You May Be Interested In

Coarse-grained simulations of concentration-dependent molecular self-assembly of Polysorbate 80 in water

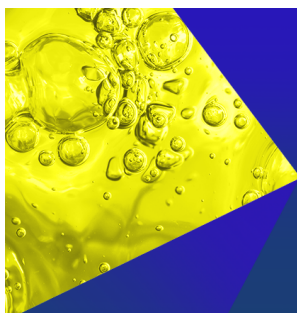
Physics of Fluids (September 2024)

Magnetic carriers of iron nanoparticles coated with a functional polymer for high throughput bioscreening

J. Appl. Phys. (April 2006)

Reoccurrence of Covid-19 infection in vaccinated Iraqi community

AIP Conf. Proc. (April 2023)



Physics of Fluids
Special Topics
Open for Submissions

[Learn More](#)

Fluid propagation and protein adsorption patterns in porous nitrocellulose membranes for lateral flow assays

Cite as: Phys. Fluids **37**, 032022 (2025); doi: [10.1063/5.0257343](https://doi.org/10.1063/5.0257343)

Submitted: 9 January 2025 · Accepted: 18 February 2025 ·

Published Online: 11 March 2025



View Online



Export Citation



CrossMark

Alexander Spreinat,^{1,2,a)} Willfried Kunz,³ Christian H. Maack,¹ Carola Wilczek,¹ Britta Nestler,^{3,4} and Andrea Ernst¹

AFFILIATIONS

¹Sartorius Stedim Biotech GmbH, August-Spindler-Straße 11, 37079 Göttingen, Germany

²Leibniz University Hannover, Institute of Technical Chemistry, Callinstraße 5, 30167 Hannover, Germany

³Karlsruhe University of Applied Sciences, Institute of Digital Materials Science, Moltkestraße 30, 76133 Karlsruhe, Germany

⁴Karlsruhe Institute of Technology (KIT), Institute for Applied Materials—Microstructure Modelling and Simulation, Strasse am Forum 7, 76131 Karlsruhe, Germany

^{a)}Author to whom correspondence should be addressed: alexander.spreinat@iftc.uni-hannover.de

ABSTRACT

Lateral flow assays (LFAs) have caught new attention in recent years due to extensive use in the containment of the COVID-19 pandemic. Especially the protein and fluid interactions with the nitrocellulose membrane structure are yet to be fully investigated, which affect the fluid and protein distribution of the test and control lines differently due to different adsorptive properties of fluids and proteins. Therefore, the relationship between fluid spread and protein distribution, respectively, and structure needs systematic evaluation. Two procedures were developed based on passive adsorption of complementary fluorescent dyes to investigate these phenomena. These procedures enabled three-dimensional visualization of the membrane structure, fluid as well as the protein spreading, respectively. Confocal laser scanning microscopy was applied after depositing picoliter and nanoliter volumes of the printing buffers containing fluorophore-labeled proteins (immunoglobulin G) and Oregon Green[™] 488 onto the membrane using a high precision micro dispenser. The resulting data were correlated with the membrane's tortuosity and permeability. Inverse-proportional dependencies for the lateral spread of the fluid and protein adsorption with the structural parameters were observed. Additionally, surfactants [polysorbate 80 (PS80) and sodium dodecylbenzenesulfonate (SDBS), both at 0.1%] were added individually to the buffers, and the spread of the liquids was evaluated. Both surfactants increase the similarities between fluid and protein shape compared to the reference data. While SDBS increases the general lateral spread, PS80 does increase the penetration depth of the protein into the membrane, which could lead to reduced signal in LFAs.

© 2025 Author(s). All article content, except where otherwise noted, is licensed under a Creative Commons Attribution (CC BY) license (<https://creativecommons.org/licenses/by/4.0/>). <https://doi.org/10.1063/5.0257343>

I. INTRODUCTION

Lateral flow assays (LFAs) are well established tools for rapid and simple point-of-care diagnostics.^{1,2} Their applications reach from the use in everyday households as pregnancy tests³ up to diagnostics in professional medical facilities.⁴ Due to the low cost and easy usability,⁵ this system became a champion of diagnostics in the COVID-19 pandemic.⁶ Chemically, the formation of sandwich complexes consisting of immobilized antibodies on the test- and control line, the respective antigen or analyte molecule and another corresponding antibody bound to a colored particle, the bead, is the foundation of LFAs.^{1,5} This general principle is well understood and is used for many

different antigen/antibody systems.^{7,8} Its robustness against slight variations in the antigen has proven to be very valuable, for instance, when one is dealing with rapidly mutating viruses.⁹

While most application-relevant factors are well understood, some underlying fundamental processes are still unknown, such as the details behind the fluid propagation and consequently protein line formation in the porous membrane structure. Past studies often focused on discovering new antibody-antigen-systems,^{10,11} establishing new LFA-applications for different analytes^{12–14} as well as for improved and more sensitive diagnostics.^{15–17} On a more fundamental level, computational studies have been conducted^{18–21} and a deeper

understanding of the protein line printing was generated.²² Experimentally, porous membranes have proven to be a challenging material to investigate time- and space-resolved protein adsorption,²³ which typically results in experimental settings in lower special resolutions.²⁴ To understand the processes happening during fluid and protein distribution inside the membrane, it is inevitable to explore methods that can investigate at least partially the propagation of fluids and distribution of proteins within the membrane. To achieve that, a combined computational and confocal laser scanning microscopy (CLSM) approach has been used. To generate the experimental data, two new procedures were developed, which enabled imaging the membrane structure, the droplets of protein, and the buffer fluid at the same time. The first procedure was based on passive adsorption of protein-bound fluorophores to stain the membrane thoroughly and a high precision micro dispensing unit to apply picoliter volumes of liquid containing a small molecule fluorescent dye or a protein-bound fluorescent dye, both with complementary emission wavelengths with regard to the membrane staining. The membrane staining was used to generate structural data on a micrometer level, while the data from the droplets lead to the spread. The other new procedure was used to generate droplet data from the adsorption buffer and applied protein droplets simultaneously by applying a mixture of a protein-bound fluorescent dye and a complementary small molecule fluorescent dye to study differences and similarities in protein and fluid interaction with the membrane structure. The procedures are described in detail in Sec. III A. These two methods are capable to image different states of the processes in the membrane and to get an idea of how and when the fluid propagation of either the simple fluid or the protein correlates and what might constitute the correlation both structurally and chemically.

II. MATERIALS AND METHODS

The experiments were conducted using nitrocellulose (NC) membranes provided by Sartorius Stedim Biotech GmbH. The average properties of the used membranes are given in Table I.

A. Confocal laser scanning microscopy

Small pieces of membrane were used for CLSM experiments, which were labeled prior to the different investigations using either IgG-bound Alexa Flour®-dyes or protein-free Oregon Green™ 488. The staining procedures varied for the different experimental approaches and are described in Secs. II B and III A. In order to image the NC-pieces, the samples were deposited on a microscope slide ($75 \times 25 \times 1 \text{ mm}^3$) and coated with an immersion oil with a refraction index of 1.5251, which comes close to typical cellulose materials of 1.477,²⁵ in order to achieve transparency for the sample and to enable the acquisition of 3D image stacks through the whole membrane. Typical pixel sizes varied. The microscope was an upright Leica TCS SPE, equipped with a 10x air objective (Leica HC PL Fluotar 10×/0.3),

a 40× air objective (Leica HC PL Fluotar 40×/0.8), and a 63× oil objective (HC PL APO 63×/1.4–0.6 Oil). The samples were excited using a solid-state laser with the excitation wavelengths 488/561/635 nm. The detector of the microscope was a photo multiplier tube. Z-stacks were acquired using a galvanometric stage with a precision of 250 nm.

B. Dyeing whole membranes

To visualize the porous membrane structure, depending on the experimental requirements, two different dyeing procedures were used. To dye small membrane pieces (up to $1.0 \times 0.5 \text{ cm}^2$), a well-established staining protocol was used. The piece of membrane was dried at 50 °C for at least 2 h in an oven at ambient pressure and atmosphere. Afterward, the IgG-bound dye of interest (Invitrogen Alexa Fluor™ 555 goat anti-mouse IgG (H + L), Thermo Fisher, A21422/Invitrogen Alexa Fluor 647 goat anti-mouse IgG (H + L), Thermo Fisher, A21235/Invitrogen Alexa Fluor 488 goat anti-mouse IgG (H + L), Thermo Fisher, A11059) were diluted to a concentration of 40 μg/ml in an adsorption buffer (pH = 8.0, 50 mM borate, 150 mM NaCl, and 1% sucrose). The membrane (approximately 0.5 cm²) was then incubated in 1.5 ml of the dye solution for about 48 h at 7 °C. After that time, the membrane was removed from the solution and again dried at 50 °C in an oven for 2 h. However, for dyeing larger membrane parts (up to $7.5 \times 2.1 \text{ cm}^2$), this procedure was modified. The membrane was dried for 2 h at 50 °C in an oven (under ambient pressure and atmosphere), subsequently, the membrane was placed in a 50-ml falcon tube. 10 ml of a solution of the IgG-bound Alexa Fluor-dye at a concentration of 40 μg/ml was added to this tube and the tube was rotated at 7 °C for 48 h. After that, the membrane piece was removed and dried a second time for 2 h at 50 °C under ambient pressure and atmosphere.

C. Spotting pico- to nanoliter droplets

For applying smallest amounts of dye liquids, a Scienion micro-dispensing unit (Scienion Spotter sciFLEXARRAER S3), equipped with a piezo dispense capillary (PDC 90 Piezo Dispense Capillary, S3) was used. Volumes with fractions of 400 pl were added to the membranes stepwise. A camera integrated into the spotter was used to control the shape and size of the droplets. The whole device was positioned in a glass chamber with humidity control (50%). The membranes were spotted using either a solution of IgG-bound Alexa Fluor dyes (described in Sec. II B) or a solution of Oregon Green 488 (Oregon Green 488 Maleimide, Thermo Fisher, O6034). The used concentrations were 20 μg/ml for the Alexa Fluor dyes and 100 μg/ml for Oregon Green 488. Different patterns of droplets were spotted onto the membranes and afterward recorded as 3D-Stacks using a confocal microscope, as described in Sec. II A.

D. Computational membrane structure analysis

A 3D digital twin of the fully resolved membrane structure was generated from a CLSM image stack. Prior to 3D reconstruction, the image stack underwent pre-processing. To compensate for an observed intensity gradient across the membrane thickness, each image was normalized by its maximum gray value. Subsequently, a Gaussian filter with a standard deviation of $\sigma = 450 \text{ nm}$ was applied, following the approach of Altschuh *et al.*²⁶ Image segmentation into foreground

TABLE I. Properties of the employed membrane type.

Membrane thickness without backing (μm)	Porosity (%)	Mean pore size (μm)	100 μm backing	Capillary flow time/s/40 mm
120–145	84.0 ± 1	4.4 ± 0.2	Yes	95–155

(structure) and background (pores) was achieved by thresholding, with the threshold corresponding to the experimentally determined porosity described in Sec. II E. This segmentation method is described in detail by Ley *et al.*²⁷ The segmented images were subsequently meshed to form a 3D voxelized digital twin (as shown in Fig. 4). The pre-processing and thresholding were performed by using the open-source image processing program ImageJ 1.53.²⁸

The obtained 3D digital twin of the membrane structure was subsequently utilized to determine permeability and tortuosity in lateral directions using the simulation framework Pace3D.²⁹ Permeabilities were calculated by conducting single-phase fluid flow simulations within the pore space and applying Darcy's Law³⁰ as further described and validated by Kunz *et al.*³¹ Directional-dependent tortuosity is determined through simulated calculations of the electric potential within the pore space of the porous structure. The specific procedure for calculating tortuosity and the validation of the algorithm are outlined by Altschuh³² and Hofroge *et al.*³³

E. Porosity determination

To evaluate the porosity of the membranes, membrane pieces ($4.1 \text{ cm} \times 0.5 \text{ cm} \times \text{individual membrane thickness}$) were prepared, and the individual membrane height was measured using a thickness gauge. Afterward, the membrane was weighed in a moisture balance (Sartorius MA 100C) until no mass loss was observed. With the known density (ρ_{NC}) of the material of 1.82 g/ml (measured according to DIN 66137 by 3P Instruments), the volume of solid structure within the membrane cuboid can be calculated. For membranes with backing, the thickness of $100 \mu\text{m}$ backing and the corresponding mass must be subtracted in advance.

$$V_{\text{NC}} = m_{\text{dry}} / (\rho_{\text{NC}}). \quad (1)$$

The calculated volume of the material structure is given by V_{NC} , where m_{dry} is the final mass of the dry membrane and ρ_{NC} is the density. With this definition and the volume of the membrane piece V_{membrane} , the porosity P can be obtained by

$$P = (V_{\text{membrane}} - V_{\text{NC}}) / V_{\text{membrane}}. \quad (2)$$

III. RESULTS

To evaluate the relationship between porous structure and fluid spread, a series of picoliter droplets was applied to the membrane and the porous structure was investigated using Pace3D, an established software for membrane structure analysis described in Sec. IID. This approach enables the extraction of structural properties, such as pore size distribution and direction dependent characteristics as tortuosity and permeability. Since it exclusively relies on the dyed structure, which represents the dimensions of the droplets, this structure analysis is independent of the exact fluid properties and can, therefore, be used for fluids with a variety of properties. Subsequently, the spread in the lateral directions was correlated with the tortuosity and the permeability. We hypothesized that a higher tortuosity, characterized by a more convoluted path, limits the fluid propagation. The tortuosity is a geometrical parameter that only takes the physical structure into account. Additionally, a more pronounced fluid spread is expected for higher permeability, which is a measure of a porous structure's ability to allow fluids to pass through it.

Furthermore, larger volumes containing both a small fluorescent molecule as a dye, Oregon Green 488, as well as protein bound dye, IgG-Alexa647, were spotted at volumes of 400, 2000, and 20 000 pl. The two different dyes resulted in two signals (depending on the wavelength of the respective dye) and were recorded separately. Unlike proteins, protein-free Oregon Green does not adsorb as fast to the NC membrane. Therefore, it can be assumed that the molecules will stay mostly at the edge of the fluid front. The IgG-Alexa647 signal was attributed to the protein distribution of the antibody. By doing so, different spreads and signal distributions can be seen from the final protein droplet compared to the fluid droplet (Fig. 1). In order to see the influence of surfactants, which are known to change protein-surface-interactions^{34,35} on protein and fluid distribution in the membrane, sodium dodecylbenzene sulfonate (SDBS) and polysorbate 80 (PS80) were added to the printing buffer. Surfactants are commonly used in LFAs;⁵ therefore, they have been chosen as additives in this study. For easier readability, the Oregon Green 488-data will, from now on, be referred to as OG488-data and the IgG-Alexa-data will be referred to as Ax-data with the emission maxima added as number.

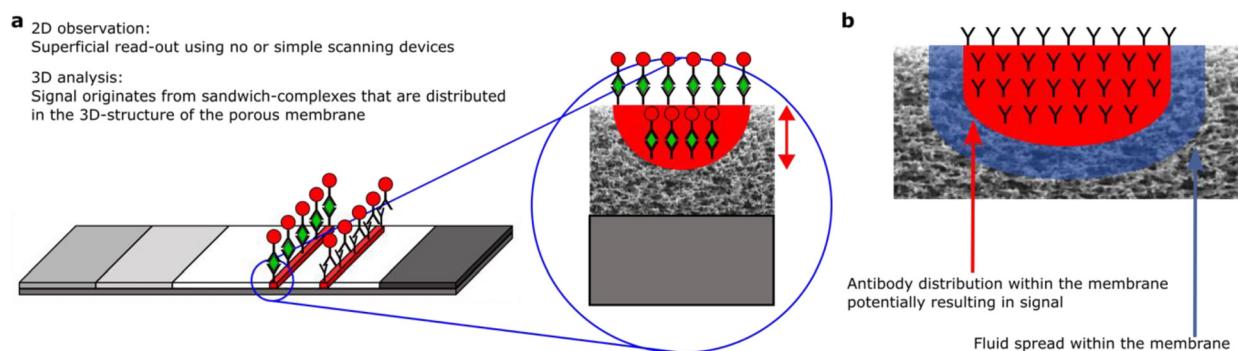


FIG. 1. Fluid and protein distribution in the membranes. (a) shows the signal determination in LFAs. While the typical readout of a lateral flow assay happens either via eye or using a custom-made scanner that typically provides top down 2D information, the reality of the binding conjugate is a 3D distribution corresponding to the antibody distribution within the membrane. (b) explains the differences between fluid and protein spread in the depth of the membrane. The spread of the antibody-line that is printed is not necessarily equivalent to the fluid spread that is observed using the bare eye. This discrepancy can lead to misinterpretations during printing and standard quality control procedures, such as printing non-protein dye lines onto the membrane.

A. Investigating fluid propagation and protein distribution

In the past, many studies focused on the analysis of the porous structure. While the structural analysis of various porous materials, such as sandstone,³⁷ calcium carbonate,³⁸ and similar materials,^{39,40} has been achieved using methods such as x-ray tomography^{37,40,41} or high-speed imaging,⁴² a comparatively simple, quantitative method for diagnostic membranes with high spatial resolution was established by Ley *et al.* in 2018.²⁷ This approach was very successful in achieving highly resolved membranes and structure parameters. However, the analysis was limited to the membrane itself and due to the necessity of applying immersion oil to the substrate to enable the imaging process, the imaging of any fluid movement in the membrane was disabled. Another drawback of the method described by Ley *et al.* is that the dyeing process in their study was based on covalent functionalization, which typically results in a more consistent and reliable signal, is more time consuming and takes more effort than a simple passive adsorption process. Moreover, it cannot be used to mimic the propagation of a fluid. However, the fluid movement can be approximated using the remains of a fluid droplet in the membrane, which can mark the borders of a spread fluid. It is important to consider the following limiting factors when planning for experimental investigation of fluid propagation in a porous diagnostic membrane: first, the applied volumes must

be small to guarantee a realistic time of calculation for the structural parameters. This limits the size of the droplet to a cube with an edge size of approximately $200\text{ }\mu\text{m}$. Second, there is a practical limitation when it comes to applying the droplets to the membrane. Since the process that dyes the membrane structure includes a 48 h incubation time in an aqueous solution, previously applied dyes which do not adsorb strongly to the membrane, such as Oregon Green are washed off. Therefore, the membrane must be dyed first.

However, the procedure developed by Ley *et al.* focusses on membrane pieces with a diameter of 10 mm (79 mm^2), which are typically too small to be properly placed to create spots of the size necessary for this experiment, since the machines require ideally pieces of a size of $75\text{ mm} \times 25\text{ mm}$ (1875 mm^2). These larger pieces use is due to their larger area almost 24 times the amount of dye using the current procedure. Even cutting the pieces in half results in 12 times the amount of dye. Trials of placing the membrane in a small petri dish ($d = 5\text{ cm}$) and adding 5–10 ml of dying solution ended up with a very heterogeneous staining of the membrane, as shown in Fig. 2(a). To ensure a homogenous staining while maintaining a reasonable consumption of resources, a procedure was developed in which the membrane was rotated for 48 to 72 h at 8°C in 10 ml of Ax647-dyeing solution in a falcon tube at a rotation speed of 30 rpm. This resulted in a sufficiently homogeneously stained membrane, as can be seen in

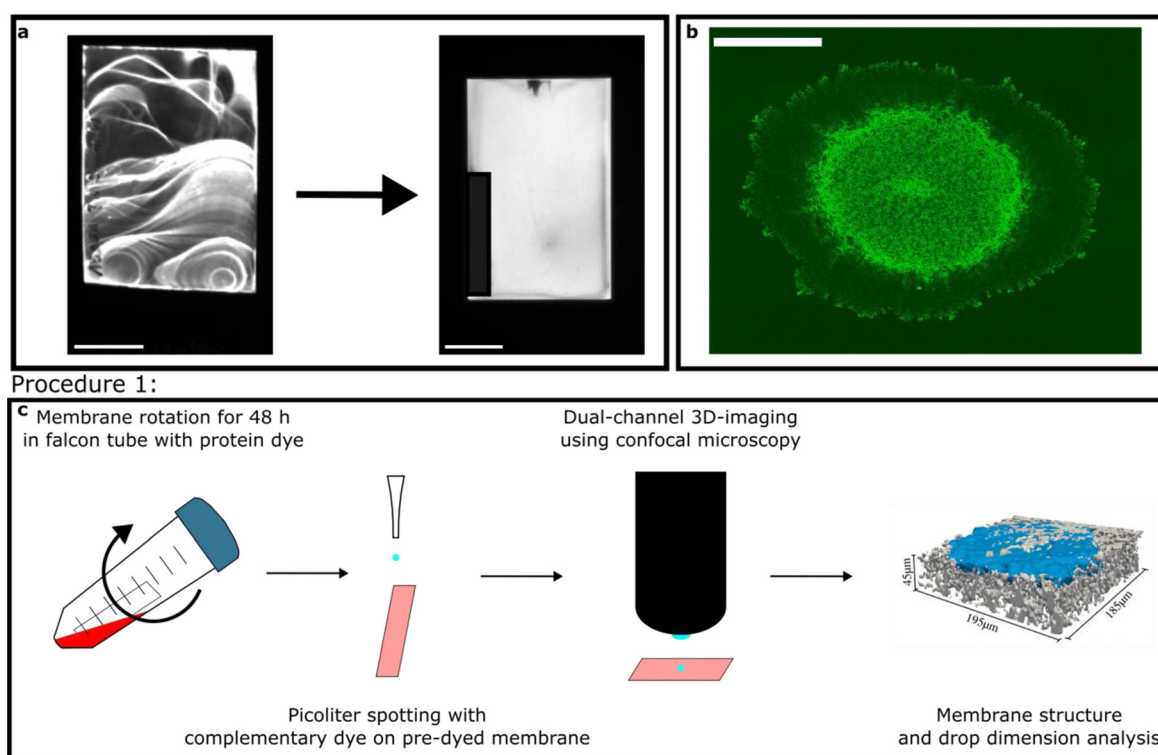


FIG. 2. Overview of preliminary experiments and first considerations. (a) visualizes the progress in dyeing large sheets of membrane that enabled the establishment of simultaneously staining the whole membrane structure while adding complementary dyed droplets. Scale bars equal $1000\text{ }\mu\text{m}$. (b) shows a 100 nl droplet of buffer solution containing Alexa Fluor555-IgG (Ax). Two different regions can be separated clearly, a more intense signal in the middle and a lesser pronounced border with a larger spread. Scale bar equals $500\text{ }\mu\text{m}$. (c) shows the workflow of procedure 1 that was applied to dye the membrane structure and afterward to apply the fluid/protein droplet to investigate the relationship between structural properties and fluid spread, and protein distribution experimentally. More details on the droplet identification are shown in the Fig. S1 of the supplementary material. Right graphic adapted from Ref. 36.

Fig. 2(a) both in lateral directions as well as with regard to penetration depth. The CLSM imaging method furthermore prevented a depth dependence of the signal intensity. These pieces of membrane were taken and spotted with the adsorption buffer containing OG488 at a concentration of 0.1 mg/ml. Protein and fluid spread data were generated using a fluorescent protein dye, based on an IgG-conjugated Alexa Fluor 488 and a small molecule dye, Oregon Green 488[®] in combination with another protein-based dye with complementary emission at 647 nm. Smallest volumes were applied (~ 400 pL) to derive a structure-spread-relation on the micrometer scale. The two fluorescence signals of the membrane and the droplet were separated afterward using two different optical configurations at the CLSM. The final processing chain of dyeing is shown in detail in Fig. 2(c) as procedure 1. Preliminary experiments spotting 100 nL of an Ax555-dye onto a membrane [Fig. 2(b)] revealed that the signal resulting from protein droplets is twofold: On one site, the droplet results in a very pronounced and intense signal directly in the middle of the droplet, and on the other side, there is an outer edge, which shows less intensity than the inner signal. It can be assumed that the outer signal results from labeled protein that does not bind fast to the NC-structure and represents the fluid front. This was further confirmed by experiments that placed OG488-spots and Ax555-spots at both the upper (air side) and the lower side (belt side) of a NC membrane. The data are shown in Fig. 3(a). This leads to the assumption that the fluid spread differs significantly from the protein adsorption and resulting distribution. The

optical impression was also confirmed in quantitative intensity profiles of the droplets [Fig. 3(a)]. To differentiate between fluid and protein signal, a mixture of complementary colored fluorophores for fluid spread and protein distribution can be applied simultaneously and afterward spectrally separated as it is shown in Fig. 3(b). In the past, different distributions of intensity profiles with pronounced intensities at the edges were referred to as coffee ring effect.⁴⁴ The coffee ring effect was described and investigated several times on porous^{44,45} and nonporous structures;⁴⁶ however, the systematic difference between fluid front of the adsorption buffer and the protein distribution has not been investigated experimentally in NC membranes for diagnostics. Therefore, procedure 2 was established which is pictured schematically in Fig. 3(c). On a larger scale, spots up to 20 nL containing OG488 and Ax647 have been applied. To understand the difference of the fluid spread and the protein distribution, a mixture of the Ax647-dye and the OG488-dye was dispensed onto an unstained membrane and afterward the fluid signal was separated from the protein signal using two different CLSM configurations that separate the two spectral signals. By doing so, the difference between fluid and protein distribution in larger volumes which are closer to the volumes used for antibody lines in a lateral flow application was observed. Furthermore, the spotting buffer has been modified with two different surfactants, sodium dodecylbenzene sulfonate (SDBS) and polysorbate 80 (PS80), to understand the influence on both the fluid spread and the protein distribution of these for LFA-applications relevant substances.

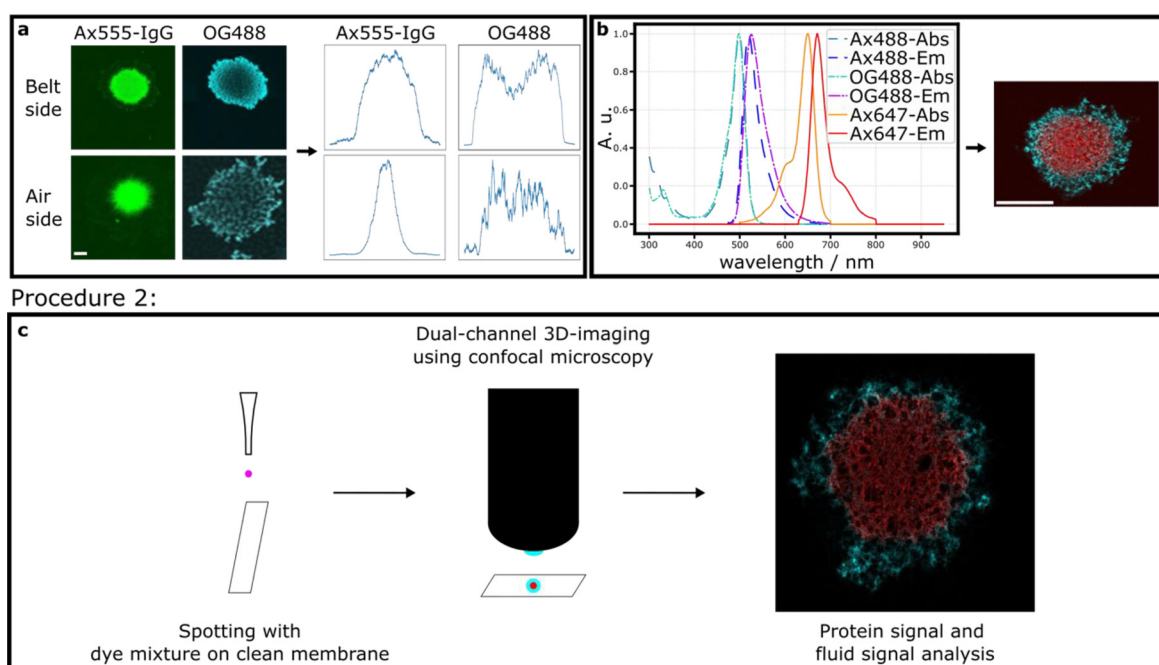


FIG. 3. Qualitative differences between protein distribution and fluid spread and selection of complementary dyes. (a) displays spotted droplets of both Ax-droplets and an additional signal from a droplet containing Oregon Green 488 (OG488-droplets), with the intensity profile alongside the x-axis of the image. Scale bar equals 100 μm . (b) illustrates the absorption and emission spectra of the used fluorophores and a combined dual channel image of a droplet containing a mixture of OG488 and Ax647, adapted from the Thermo Fisher Spectral Viewer Homepage.⁴³ Scale bar equals 100 μm . (c) shows procedure 2, which was used to dispense larger volume droplets of a mixture of OG488 and Ax647-IgG onto the membrane to explore protein distribution relative to fluid spread for larger volumes simultaneously. The red color indicates the staining by Ax647, while the blue color indicates the OG488.

B. Structure and protein/fluid interaction

Using procedure 1, the following data were acquired to find a relationship between structural properties and fluid spread, or protein distribution, respectively. Previous studies for polymer solution droplets already suggested a correlation between the permeability and the fluid spread in printer applications on ceramic powders.⁴² Consequently, a series of different studies that simulate fluid spread have been conducted,^{47–49} as well as experimental studies that focused on other porous materials, such as paper,⁵⁰ or different kinds of powder beds⁵¹ and metals.⁵² In another set of studies, the focus was set on NC-membrane-water-interaction.^{53,54} However, the experimental data that had been collected showed lower resolution in comparison with CLSM data. The adsorption process leading to the protein distribution is a combination of contact time with the membrane surface and the adsorption rate of the protein toward the specific material and the specific condition. Therefore, while the protein distribution correlates with the fluid spread, it is not the only determining factor. To investigate potential differences in relationships between structure and fluid spread, and structure and protein spread, respectively, procedure 1 was used to investigate protein and fluid shapes with regard to the membrane structure.

In Fig. 4, the experimental data from the single droplet data of both the single fluid droplet and the single protein droplet are presented. As described in Sec. III A, single droplets containing either OG488 or Ax488 have been spotted onto a previously with Ax647 dyed membrane. After that, the membrane and droplet structures were imaged using CLSM. For these experiments, the resolution was 160 nm per pixel and the signal to noise ratio (SNR) was around 50. The applied volume was set in the spotter to 400 pL, which was confirmed by controlling the volume within the membrane that was

identified computationally within the calculation process. The volume spread in the xy-plane was correlated afterward with the tortuosity, a purely geometrical parameter, which describes the curvature of a path in porous media, and the permeability, a measure of a porous structure's ability to allow fluids to pass through it, in the x- and y-direction. Here, the x-direction corresponds for all presented data in this study to the machine direction, while the y-direction corresponds to the transverse direction. As can be seen for the data from the fluid droplets, 75% of the data points correspond to the assumption that larger tortuosities correspond to smaller spreads, while larger permeabilities correspond to larger spreads of the fluid. Relevant insights into the relationship between fluid spread and tortuosity can be found in the work by Cai and Yu.⁵⁵ They demonstrated that tortuosity increases flow resistance by lengthening flow paths, thereby reducing fluid propagation in porous media. Their modified model of the Lucas-Washburn equation explicitly accounts for tortuosity, showing how it inversely affects capillary rise and fluid spread. These findings align well with the observed inverse relationship between fluid spread and tortuosity in this study. The same general trend can be observed for the data resulting from the protein droplet shown in the Figs. 4(c) and 4(d). The variance of the data is most likely due to heterogeneities of droplet formation and droplet impact during the spotting process and minor heterogeneities on the membrane surface.

C. Fluid spread and additives

To investigate the relationship between buffer or fluid spread and the corresponding protein distribution, procedure 2 was applied. Different from the experimental design of Sec. III B, more than one droplet was spotted onto a single position. This happened to increase the spread volume, so that the three investigated volumes are 400,

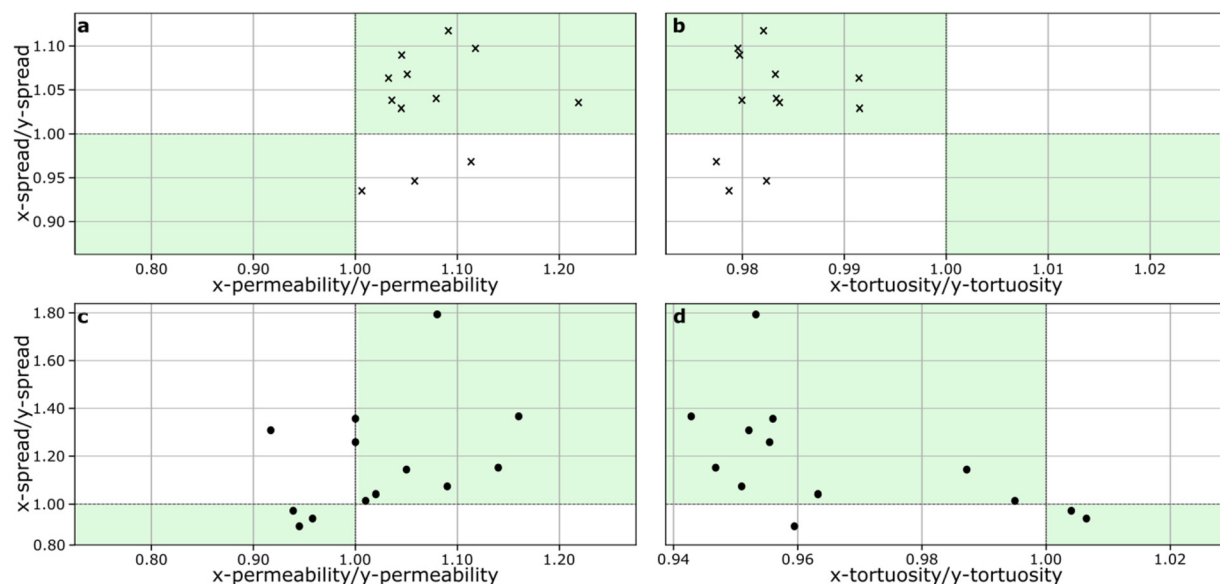


FIG. 4. Visualization of the ratio of the fluid spread (a + b) from OG488 and protein spread (c + d) from Ax488 in x- and y-direction correlated with the tortuosity (a) and the permeability (b) in the specific direction. (c) and (d) show the ratio of the x/y-permeability and the ratio of the x/y-tortuosity for the protein spread, respectively. The errors of the single data points result from measurement inaccuracies with regard to the resolution of the CLSM and are typically about 0.01 for the ratio of the spreads as well as for the calculated ratios of the tortuosities and permeabilities and are, therefore, left out for better visibility of the data points. The green colored quadrants mark the data regions, where the data correspond to the formulated hypothesis, which means that spread ratios >1 correspond to tortuosity ratios <1 and permeability ratios >1 and vice versa.

TABLE II. Fluid spread.

	Reference (μm)	SDBS (μm)	PS80 (μm)
400 pl, x-direction	201 ± 5	208 ± 9	205 ± 7
400 pl, y-direction	179 ± 3	184 ± 4	189 ± 3
2 000 pl, x-direction	343 ± 20	360 ± 7	339 ± 15
2 000 pl, y-direction	283 ± 10	345 ± 15	281 ± 10
20 000 pl, x-direction	735 ± 15	754 ± 16	684 ± 15
20 000 pl, y-direction	605 ± 1	721 ± 43	550 ± 15

2000, and 20 000 pl. In this setup, the resolution was about 490 nm per pixel, with signal to noise ratios between 7 and 20 for the protein signal and around 50 for the fluid signal. Also, the data acquired in this section include three different buffer compositions, the standard buffer used in Sec. III B, the second buffer included 0.1% SDBS, and the third variant was modified with 0.1% PS80. Afterward, a dual channel stack of the two different signals was acquired using CLSM and the border for the fluid droplet was determined. For this, the data were normalized by subtracting the background intensity and afterward dividing by background intensity. The background intensity was calculated by selecting the lowest average intensity of the single xy-planes of the image stack. After the intensities were corrected for the 3D-data of the fluid signal, the average signal intensities alongside the x- and y-direction were calculated, in order to get the droplet profiles in x- and y-direction. These profiles were smoothened by calculating the rolling average over the last five values. Afterward, the borders of the droplet were calculated by finding ten consecutive rising values in the x- and y- profiles, approaching the profiles from both sides. These borders mark the beginning and the end of the droplet dimensions. This procedure is also shown in detail in the supplementary material in Fig. S3. The calculated dimensions are shown in Table II and Fig. 5.

Figure 5 shows the spreads of the droplets of fluid for the different applied volumes in both, the x-direction [Fig. 5(a)] and the y-direction [Fig. 5(b)] for the three buffers as well as the ratio of these two measurements [Fig. 5(c)]. Additionally, the exact data are also given in Table II for a more detailed overview. Spread is defined as the total width of the droplet in the specific direction. The reference buffer without any

additives shows for 400 pl a spread in x-direction of $201 \mu\text{m} \pm 5 \mu\text{m}$, which does not change significantly after the addition of SDBS ($208 \mu\text{m} \pm 9 \mu\text{m}$) or PS80 ($205 \mu\text{m} \pm 7 \mu\text{m}$). For the spread in y-direction, it is slightly smaller compared to the x-spread for the reference buffer ($179 \mu\text{m} \pm 3 \mu\text{m}$) and the buffer containing 0.1% SDBS ($184 \mu\text{m} \pm 4 \mu\text{m}$) as well as for the buffer containing 0.1% PS80 ($189 \mu\text{m} \pm 3 \mu\text{m}$). This trend between the different buffers can be seen as well in the data for the volumes of 2000 pl, with x-spreads between $360 \mu\text{m} \pm 6 \mu\text{m}$ for SDBS, and $339 \mu\text{m} \pm 15 \mu\text{m}$ for the buffer containing PS80. The y-spreads for a volume of 2000 pl range from $281 \mu\text{m} \pm 10 \mu\text{m}$ for PS80 to $345 \mu\text{m} \pm 15 \mu\text{m}$ for SDBS. For an applied volume of 20 000 pl, a significant difference in spread in x-direction for the SDBS and the reference buffer relative to the PS80 condition can be observed ($735 \mu\text{m} \pm 15 \mu\text{m}$ for the reference condition, $754 \mu\text{m} \pm 16 \mu\text{m}$ for the SDBS condition and $684 \mu\text{m} \pm 15 \mu\text{m}$ for the PS80 condition). The y-spread for the buffer containing 0.1% PS80 is at this volume $550 \mu\text{m} \pm 15 \mu\text{m}$, which is the lowest observed spread compared to the spread of the reference buffer with $605 \mu\text{m} \pm 1 \mu\text{m}$ and the spread of the SDBS condition $721 \mu\text{m} \pm 43 \mu\text{m}$. The ratios of the x- and y-spreads for the three different buffers stay consistent over the whole volume range. For the reference buffer, it varies between 1.2 ± 0.1 for 2000 pl and 1.1 ± 0.05 for 400 pl, which are within each other's errors, while the ratios for the spotting buffer containing 0.1% SDBS vary between 1.1 ± 0.1 for 400 pl and 1.0 ± 0.1 for 20 000 pl. The spotting buffer containing 0.1% PS80 shows a ratio between 1.1 ± 0.1 for 400 pl and 1.2 ± 0.1 for 20 000 pl. In general, the shapes are not perfectly circular but show a distortion in x-direction. Generally, the addition of SDBS seem to increase the general spread of the fluid with a more pronounced increase in y-direction, which makes the droplets shape in general more symmetrical.

D. Fluid and protein signal distributions for larger volumes

In the next step, the previously with regard to the dimensions of the fluid spread analyzed droplet data were further investigated more deeply with a focus on protein distribution and penetration depth. Example images of the two droplet signals are given for all the three buffer types in Fig. 6(a). After the spreading dimensions for every droplet were calculated, these dimensions were used to normalize the signals of the protein and fluid, respectively. It was assumed that no

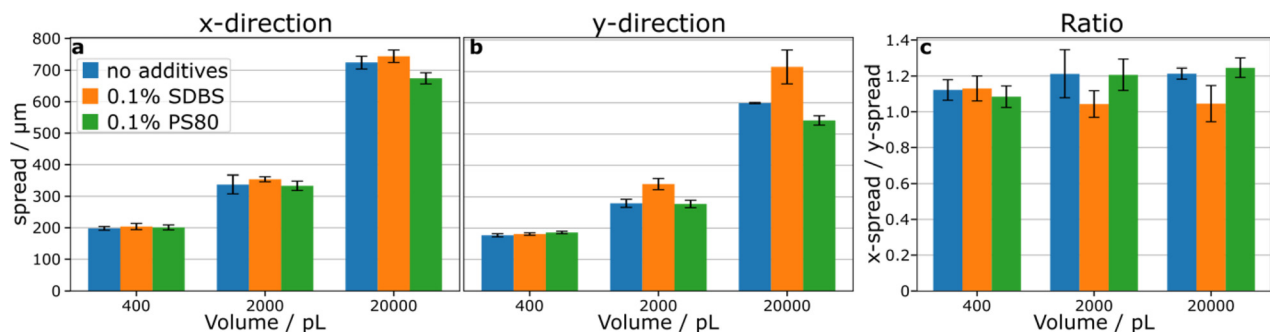


FIG. 5. Fluid spread borders with regard to different applied volumes and additives. (a) shows the spread of the droplets in x-direction for the volumes 400, 2000, and for 20 000 pl for the reference buffer without any additives, the reference buffer with 0.1% PS80, and 0.1% SDBS. Number of individual experiments (n) = 3, error = standard deviation (SD). (b) shows the spread of the fluid droplet in y-direction for the same conditions described before. n = 3, error = SD. In 5(c), the ratios of the x- and y-direction spread for the three buffer variations and the three volumes are shown.

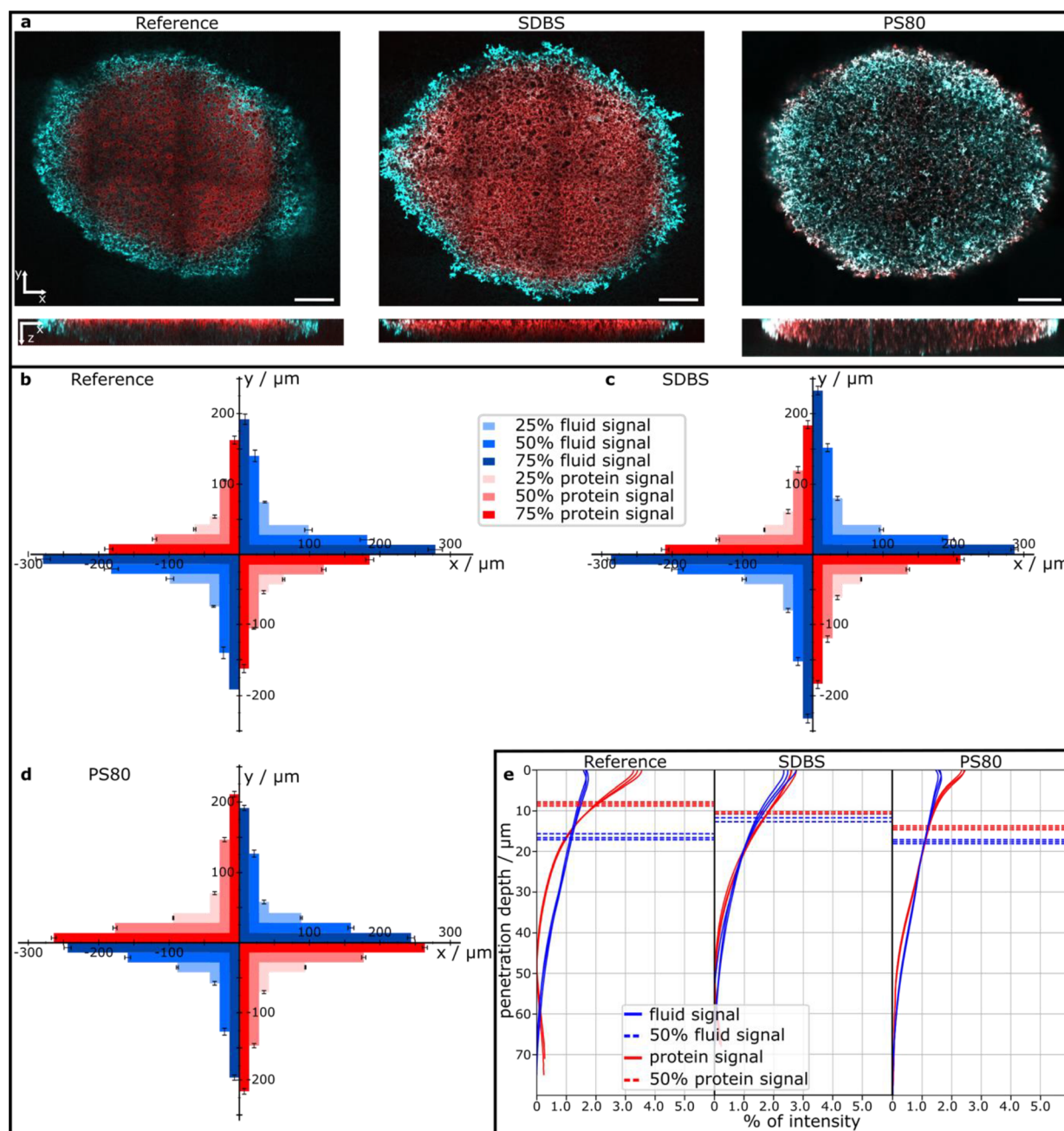


FIG. 6. Representative images of analyzed droplets and distribution of the fluid and protein signal for the three different buffers in xy-plane and z-direction for the 20 000 pL volume. Figure 6(a) shows example data for the analyzed droplets. The data are for illustrative purposes only and should not be interpreted quantitatively from these images only. The scale bars equal 100 μm . For (b)–(d), the red(ish) colors correspond to the protein signal distribution according to the different thresholds of 25%, 50%, and 75%. The blue(ish) colors show the fluid distributions accordingly. (e) shows the penetration depth for the three buffers into the membrane for the fluid and protein signal, with the reference buffer in the left, the SDBS buffer in the center and the PS80 buffer in the right panel. The dotted line represents the threshold, where 50% of the signal is reached. $n = 3$, error = SD.

amount of protein could exceed the borders of the fluid droplet. Therefore, the protein signal was normalized to 100% within the borders estimated from the fluid signal. Within these borders, the signal distribution was calculated and the expansion for 25%, 50%, and 75%

of the protein signal relative to the center of the droplet calculated. In the z-direction of the stack, the different borders for the penetration depth of the signal were calculated. Due to the faster absorption of the protein compared to OG488, the upper layer of the membrane was

found using the maximal intensity in the z-profile of the protein signal. The lowest layer of the droplet was determined to be the z-slice where the fluid intensity is indistinguishable from the background noise, since it can be reasonably assumed that the fluid penetrates the membrane deeper than the protein. Uncertainties with regard to determining the limits of the droplet might be due to bleaching of the fluorescence signal which could reduce the detected penetration depth, while the upper layer can typically be detected robustly. The uncertainties should affect fluid spread and protein distribution in the same way and direction and additionally, the potential uncertainties should affect the results if at all only insignificantly. By using these data, the penetration depths have been investigated. The equivalent fluid signal distributions in the xy-plane and z-direction were calculated for comparison. In the main document, mainly the data of the 20 000 pl droplet is described in detail. The other datasets can be found in detail in the supplementary material in Figs. S4 and S5. In general, the data of the smaller volumes show comparable trends.

E. Lateral spread of fluid and protein signal

Figure 6(b)–6(d) show the lateral spread of the three different buffer conditions and for the fluid and protein signal for the volume of 20 000 pl. The spread in the x- and y-directions is depicted with respect to the x- and y-axes of the diagrams, respectively. Figure 6(b) represents the distributions for the reference buffer. Here, 50% of the fluid signal spread out to $362 \mu\text{m} \pm 20 \mu\text{m}$ in x-direction and $280 \mu\text{m} \pm 17 \mu\text{m}$ in y-direction, while the protein distribution reaches 50% at a spread of $240 \mu\text{m} \pm 6 \mu\text{m}$ in x-direction and $210 \mu\text{m}$ in y-direction. 75% of the fluid signal are located within a spread of approximately $400 \mu\text{m}$ in y direction and $550 \mu\text{m}$ in x-direction, respectively. Compared to that, the protein distribution reaches 75% at a spread of $370 \mu\text{m}$ in x-direction and $320 \mu\text{m}$ in y-direction. For the data from the buffer containing 0.1% SDBS, similar trends with regard to the xy-spread for the protein and fluid signal compared to the reference buffer can be observed; however, the spreads are in general wider than the reference buffer. The spreads for 75% of the fluid signal in x-direction equals $574 \mu\text{m} \pm 12 \mu\text{m}$ and the corresponding spread in y-direction equals $465 \pm 13 \mu\text{m}$, which is significantly more than it is observed for the reference buffer. Also, the protein signal exceeds the protein signal of the reference buffer at the 75% border with a spread of $418 \mu\text{m} \pm 11 \mu\text{m}$ in x-direction and $366 \pm 12 \mu\text{m}$ in y-direction. The buffer that contained 0.1% PS80 on the other hand shows an even larger spread for the 25%, the 50%, and the 75% thresholds for the spread of the protein signal (for protein at 25% $190 \mu\text{m} \pm 5 \mu\text{m}$, for 50% $350 \mu\text{m} \pm 10 \mu\text{m}$, and for 75% $520 \mu\text{m} \pm 10 \mu\text{m}$), while the spread for 25% of the fluid signal is $180 \mu\text{m} \pm 5 \mu\text{m}$, for 50% $310 \mu\text{m} \pm 5 \mu\text{m}$ and for 75% $480 \mu\text{m} \pm 7 \mu\text{m}$ for the x-direction and, therefore, generally smaller than the spread for the buffer containing SDBS or the reference buffer. Accordingly, the ratios for this case are the same for the protein and fluid spread for all volumes. All numbers can also be found in detail in Table S1.

F. Penetration depth of fluid and protein signal into the membrane

In addition to the lateral spread, the 3D-stacks measured using CLSM also provided a visualization of the penetration depth of the two signals. These data are shown in Fig. 6(e). For an easier

quantitative comparison, the 50% distribution border was calculated. Upon comparing the fluid and protein penetration depths, it was consistently observed that the fluid signal extended further into the membrane than the protein signal, regardless of the volume or buffer composition [see Fig. 6(e), Figs. S3(d) and S4(d)]. The data for 20 000 pl is presented in the main document in Fig. 6. For the reference buffer, 50% of the protein signal goes down to $8.5 \mu\text{m} \pm 0.5 \mu\text{m}$, while the fluid intensity distribution is shifted significantly more down into the membrane with 50% down to $16 \mu\text{m} \pm 1 \mu\text{m}$. This underlines that the protein is binding more strongly toward the membrane and, therefore, allocates more in the upper layers of the 3D-structure, while the fluid is mainly carried by capillary forces and not surface specific interactions. Comparing these results with the signal from the buffer containing 0.1% PS80, [Fig. 6(e), right panel] the penetration depth is much increased for the protein signal, which for the upper 50% increases to $14 \mu\text{m} \pm 0.5 \mu\text{m}$, while the data show a penetration depth for the first 50% of the fluid signal of $18 \pm 0.5 \mu\text{m}$ which is a smaller increase in penetration depth compared to the reference buffer. For the buffer containing 0.1% SDBS [Fig. 6(e), center panel] the penetration depth of the protein signal drops to $10 \mu\text{m} \pm 1 \mu\text{m}$, while the fluid distribution reaches 50% of the signal distribution at a depth of $12 \mu\text{m} \pm 1 \mu\text{m}$. Compared to the reference buffer, the protein penetration depth is not significantly changed, while the penetration depth of the fluid is significantly reduced. In general, a much wider lateral spread than penetration depth is observed, which agrees with theoretical models and other data from previous publications using ink and other paper media.³⁹ Furthermore, the generally increased penetration depth for the buffer containing PS80 explains the smaller lateral spread shown in Sec. III E, while the smaller penetration depth especially for the fluid signal for the buffer containing 0.1% SDBS corresponds to the larger lateral spread.

IV. DISCUSSION

We described and established novel methods to dye porous NC membranes. Furthermore, two procedures to visualize a fluid spread inside the membrane in three dimensions have been developed. Procedure 1 provides a 3D-spread analysis on a micrometer length scale in an easy and time efficient way. Procedure 2 provides both information about the fluid spread as well as the protein distribution on the microscopic level. While previous studies focused mainly on macro scale fluid propagation and signals in specific lateral flow applications, this study focuses on the structural relationship between membrane, fluid and, protein adsorption. Moreover, the influence of two common additives at applicational relevant concentrations was evaluated. First, the data visualize the xy-spread of both the protein and the fluid that introduces the protein solution to the membrane. For both these parameters, we see a significant directional dependent asymmetry. The results pictured in Sec. III B illustrate that in general the fluid spread correlates positively with the permeability, as it was mathematically predicted by Holman *et al.*⁴² and apparently the same applies with an antiproportional correlation with the measured tortuosity. Also, the protein spread, or distribution respectively, is correlated in the same way with the structural features. The signal intensity distribution for the protein signal results from two different processes. The fluid propagates through the membrane at a certain velocity that results from the capillary forces which take effect in the porous membrane. Protein adsorption to a surface is typically described by a Langmuir adsorption process,^{56–58} where the adsorption rate is

determined by the number of free binding sites, the concentration of the binding reagent in the solution, and the adsorption rate constant. However, in a propagating fluid, the propagation velocity plays a critical role in the adsorption process, since it determines the contact time with the surface and the arriving proteins follow a concentration distribution profile.^{59,60} The results presented in Sec. III B suggest that the adsorption rate in the chosen experimental setup and the protein solution configuration is slow compared to the propagation speed, since both the protein droplets and the fluid droplets show similar trends regarding the structural features as permeability and tortuosity. Going to the larger scale of protein and fluid distribution in the Secs. III C–III F, the differences in fluid and protein spread become more apparent with the protein morphology staying more symmetrical and the fluid shape becoming more oval. This shows that the larger the propagated distance becomes, the influence of the protein adsorption process rate increases and, therefore, leads to stronger differences compared to the spread of the fluid as can be seen by the ratios of x - and y -spread for the 400, the 2000, and the 20 000 pl sample. The changes observed in droplet morphology as soon as the surfactants are added indicate that both surfactants interfere with the binding reaction. The addition of SDBS leads to a more spread signal in the lateral axis for both fluid and protein, and slightly deeper penetration for the protein distribution, while the fluid penetration is reduced. This can be explained by a less concentrated but more spread protein distribution in the upper layers. Adding PS80 leads to very similar protein and fluid spread which is less spread out but shows a deeper penetration depth. Resulting from the observed interference, especially for the buffer containing PS80, the protein distribution is much closer to the fluid distribution, making the two shapes almost congruent. However, this comes at the cost of a deeper penetration of the protein compared to the penetration depth of the reference ($26.5\text{ }\mu\text{m}$ compared to $17\text{ }\mu\text{m}$ for 75% of the signal of the protein, see Table S2). Therefore, when surfactants are added to the buffer, it needs to be considered that this could lead to a reduction of potentially visible capture antibodies, which needs to be considered when buffer condition optimization is performed, since it is typically assumed that only the upper $10\text{ }\mu\text{m}$ of the binding analyte results in a visible signal.⁶¹ Another aspect that needs to be considered are changes in surface tension by the addition of the additives, which were measured additionally (using a commercially available OCA 15 Pro Contact Angle System OCA by Data Physics Instruments). The surface tension of the buffer solution changes from $73.6 \pm 0.2\text{ mN/m}$ for the pure buffer to $27.45 \pm 0.03\text{ mN/m}$ for the buffer containing 0.1% SDBS and to $45.7 \pm 0.3\text{ mN/m}$ for the buffer containing 0.1% PS80 ($n = 5$, error = SD). Corresponding to the changed surface tensions, also the contact angles change from $83 \pm 4^\circ$ for the pure buffer solution to $60 \pm 9^\circ$ for the buffer containing 0.1% SDBS and to $65 \pm 9^\circ$ for the buffer solution containing 0.1% PS80 ($n = 5$, error = SD). Although contact angles are notoriously difficult to measure on porous media, the results underline the increased wettability of the membrane by a solution containing surfactants. The changed contact angles correspond well to the larger spreads of the droplets containing SDBS. This underlines the effects observed in three dimensions and suggest that the larger spreads, especially for the buffer containing SDBS are potentially partially created at liquid application. However, for PS80, which shows a smaller spread while a larger contact angle, which is potentially due to faster absorption into the membrane, we can see that the final fluid spread and protein distribution results from

multiple factors, such as contact angle, absorption speed into the membrane and (for the protein distribution) adsorption onto the porous structure.

The experimental procedure established in this work comes with two limitations. First, the application of the volume via repeated drop dispensing does not exactly equal the diagnostic application, where a continuous line is printed to the membrane via line dispenser. The larger volumes are applied in steps of 400 pl, which does not equate to a single large droplet. However, this might change the outcome for other application procedures quantitatively compared to the procedures used in this study, but it is unlikely to change the general trends observed with regard to the relationship between structural parameters and fluid spread or the influence of the additives on the protein spread. The procedures presented in this work can easily be modified to match other application procedures. The second drawback of this work is the fact that it focuses on adsorbed proteins instead of the binding of a bead-conjugate, which is, for most cases, responsible for the signal in a lateral flow application. However, since the bead-conjugate can only bind where the adsorbed antibody line is located, this approach is insightful for at least one signal intensity limiting step in the LFA.

V. CONCLUSION

In this work, a simple, fast and resource efficient procedure was established to analyze NC membrane structure and to correlate complementary dyed fluid and protein droplets with the structural features. A variation of the established method was furthermore used to understand the differences between fluid and protein spread within a protein spotting process. These experimental results highlight structure and fluid propagation relations and the influence of surfactants on the differences between the fluid spread and the protein distribution. Especially with regard to the data of the penetration depth, it showed very small standard deviations which suggests a high reproducibility of the method. On an applicational motivated level, it is shown that by finetuning tortuosity and permeability, and their gradient in the membrane structure both the fluid and the protein distribution can be altered to optimize signal intensity. The additives change the distribution with SDBS leading to more spread-out fluid and protein, and PS80 to a deeper penetration especially of the protein. While both surfactants make the fluid spread and the protein distribution more similar, especially PS80 can help to synchronize the by optical evaluation accessible fluid spread with the resulting antibody line, leading to almost identical fluid spreads and protein distributions. Therefore, since in quality control measures often rely on the application and the observation of fluid spread and not fluorescence-labeled proteins, manufacturers of lateral flow tests could aim to optimize buffer conditions that help to synchronize fluid and protein spread. On a more methodological level, these kinds of experiments, which can compare the signal intensity distribution to the fluid spread using confocal microscopy data, can be used to develop a method to access protein adsorption rates. All in all, this work offers a valuable extension for the toolbox of the analysis of membrane structures and line printing in porous media as well as protein and fluid, and membrane interaction.

SUPPLEMENTARY MATERIAL

See the supplementary material for tables containing all protein distributions and fluid spreads for the droplet sizes in the main manuscript and smaller droplet sizes as well as detailed information on data analysis.

ACKNOWLEDGMENTS

This work was financially supported by the company Sartorius Stedim Biotech GmbH and by the German government, through the Bundesministerium für Bildung und Forschung (BMBF)/Federal Ministry of Education and Research project Multipore (Project ID. 13FH020KX0). We would like to thank Judith Witte, Patrick Altschuh, Marcel Bremerich, and Volkmar Thom for the fruitful discussions. We acknowledge the Institute of Technical Chemistry at the Leibniz University Hannover, where we would especially thank Sascha Beutel, Thomas Scheper, and Frank Stahl for the valuable input.

AUTHOR DECLARATIONS

Conflict of Interest

The authors have no conflicts to disclose.

Author Contributions

Alexander Spreinat: Conceptualization (equal); Data curation (lead); Formal analysis (equal); Investigation (equal); Methodology (equal); Writing – original draft (lead); Writing – review & editing (equal). **Willfried Kunz:** Conceptualization (equal); Formal analysis (equal); Methodology (equal); Writing – original draft (supporting); Writing – review & editing (equal). **Christian H. Maack:** Data curation (equal); Methodology (equal); Writing – review & editing (equal). **Carola Wilczek:** Conceptualization (equal); Supervision (equal); Writing – review & editing (equal). **Britta Nestler:** Supervision (equal); Writing – review & editing (equal). **Andrea Ernst:** Funding acquisition (equal); Resources (equal); Supervision (lead); Writing – review & editing (equal).

DATA AVAILABILITY

The data that support the findings of this study are available from the corresponding author upon reasonable request.

REFERENCES

- R. S. Yalow and S. A. Berson, "Immunoassay of endogenous plasma insulin in man," *J. Clin. Invest.* **39**(7), 1157–1175 (1960).
- B. Ragnosola, D. Jin, C. C. Lamb, B. H. Shaz, C. D. Hillyer, and L. L. Luchsinger, "COVID19 antibody detection using lateral flow assay tests in a cohort of convalescent plasma donors," *BMC Res. Notes* **13**(1), 372 (2020).
- B. G. Andryukov, "Six decades of lateral flow immunoassay: From determining metabolic markers to diagnosing COVID-19," *AIMS Microbiol.* **6**(3), 280–304 (2020).
- R. Aerts, L. Cuypers, T. Mercier, J. Maertens, and K. Lagrou, "Implementation of lateral flow assays for the diagnosis of invasive aspergillosis in European Hospitals: A survey from Belgium and a literature review of test performances in different patient populations," *Mycopathologia* **188**(5), 655–665 (2023).
- C. Parolo, A. Sena-Torralba, J. F. Bergua, E. Calucho, C. Fuentes-Chust, L. Hu, L. Rivas, R. Álvarez-Diduk, E. P. Nguyen, S. Cinti, D. Quesada-González, and A. Merkoçi, "Tutorial: Design and fabrication of nanoparticle-based lateral-flow immunoassays," *Nat. Protoc.* **15**(12), 3788–3816 (2020).
- R. W. Peeling, D. L. Heymann, Y.-Y. Teo, and P. J. Garcia, "Diagnostics for COVID-19: Moving from pandemic response to control," *Lancet* **399**(10326), 757–768 (2022).
- K. W. Prentice, L. DePalma, J. G. Ramage, J. Sarwar, N. Parameswaran, J. Petersen, B. Yockey, J. Young, M. Joshi, N. Thirunavukarasu, A. Singh, C. Chapman, J. R. Avila, C. A. Pillai, G. Manickam, S. K. Sharma, S. A. Morse, K. V. Venkateswaran, K. Anderson, D. R. Hodge, and S. P. Pillai, "Comprehensive laboratory evaluation of a lateral flow assay for the detection of *Yersinia pestis*," *Health Secur.* **17**(6), 439–453 (2019).
- J. G. Ramage, K. W. Prentice, L. DePalma, K. S. Venkateswaran, S. Chivukula, C. Chapman, M. Bell, S. Datta, A. Singh, A. Hoffmaster, J. Sarwar, N. Parameswaran, M. Joshi, N. Thirunavukarasu, V. Krishnan, S. Morse, J. R. Avila, S. Sharma, P. L. Estacio, L. Stanker, D. R. Hodge, and S. P. Pillai, "Comprehensive laboratory evaluation of a highly specific lateral flow assay for the presumptive identification of *Bacillus anthracis* spores in suspicious white powders and environmental samples," *Health Secur.* **14**(5), 351–365 (2016).
- H. Scheiblaue, A. Filomena, A. Nitsche, A. Puykens, V. M. Corman, C. Drosten, K. Zwirgmaier, C. Lange, P. Emmerich, M. Müller, O. Knauer, and C. M. Nübling, "Comparative sensitivity evaluation for 122 CE-marked rapid diagnostic tests for SARS-CoV-2 antigen, Germany, September 2020 to April 2021," *Eurosurveillance* **26**(44), 2100441 (2021).
- X. Wang, K. Li, D. Shi, N. Xiong, X. Jin, J. Yi, and D. Bi, "Development of an immunochromatographic lateral-flow test strip for rapid detection of sulfonamides in eggs and chicken muscles," *J. Agric. Food Chem.* **55**(6), 2072–2078 (2007).
- Y. Liu, L. Zhan, Z. Qin, J. Sackrisson, and J. C. Bischof, "Ultrasensitive and highly specific lateral flow assays for point-of-care diagnosis," *ACS Nano* **15**(3), 3593–3611 (2021).
- J. Hwang, S. Lee, and J. Choo, "Application of a SERS-based lateral flow immunoassay strip for the rapid and sensitive detection of staphylococcal enterotoxin B," *Nanoscale* **8**(22), 11418–11425 (2016).
- L. Yao, J. Teng, M. Zhu, L. Zheng, Y. Zhong, G. Liu, F. Xue, and W. Chen, "MWCNTs based high sensitive lateral flow strip biosensor for rapid determination of aqueous mercury ions," *Biosens. Bioelectron.* **85**, 331–336 (2016).
- P. P. Behera, S. K. Mehta, K. Agarwal, S. Bera, R. K. Arun, and P. K. Mondal, "Paper-based lateral flow assays: Prediction of methanol content in alcoholic beverages," *Phys. Fluids* **36**(12), 123619 (2024).
- C. A. Holstein, "Development of a novel paper-based flu test for improved diagnosis at the point of care," Ph.D. thesis (University of Washington, 2015).
- P. J. W. He, I. N. Katis, R. W. Eason, and C. L. Sones, "Rapid multiplexed detection on lateral-flow devices using a laser direct-write technique," *Biosensors* **8**(4), 97 (2018).
- B. Kalish, M. K. Tan, and H. Tsutsui, "Modifying wicking speeds in paper-based microfluidic devices by laser-etching," *Micromachines* **11**(8), 773 (2020).
- D. Gasperino, T. Baughman, H. V. Hsieh, D. Bell, and B. H. Weigl, "Improving lateral flow assay performance using computational modeling," *Annu. Rev. Anal. Chem.* **11**, 219–244 (2018).
- F. Jamshidi, W. Kunz, P. Altschuh, M. Bremerich, R. Przybylla, M. Selzer, and B. Nestler, "Geometric flow control in lateral flow assays: Macroscopic single-phase modeling," *Phys. Fluids* **34**(6), 62110 (2022).
- H. Asadi, M. Pourjafar-Chelikdani, N. P. Khabazi, and K. Sadeghy, "Quasi-steady imbibition of physiological liquids in paper-based microfluidic kits: Effect of shear-thinning," *Phys. Fluids* **34**(12), 123111 (2022).
- F. Jamshidi, S. Bayat, A. Ernst, and B. Nestler, "Geometric flow control in lateral flow assays: Macroscopic two-phase modeling," *Phys. Fluids* **36**(11), 112108 (2024).
- J. Wang, V. Thom, M. Hollas, and D. Johannsmann, "Dye deposition patterns obtained in line printing on macroporous membranes: Improvement of line sharpness by liquid redistribution," *J. Membr. Sci.* **318**(1), 280–287 (2008).
- N. Ideris, A. L. Ahmad, B. S. Ooi, and S. C. Low, "Correlation study of PVDF membrane morphology with protein adsorption: Quantitative analysis by FTIR/ATR technique," *IOP Conf. Ser.: Mater. Sci. Eng.* **358**(1), 012054 (2018).
- P. P. Behera, S. K. Mehta, R. K. Arun, and P. K. Mondal, "Solute imbibition in paper strip: Pore-scale insights into the concentration-dependent permeability," *Phys. Fluids* **35**(12), 122007 (2023).
- S. N. Kasarova, N. G. Sultanova, C. D. Ivanov, and I. D. Nikolov, "Analysis of the dispersion of optical plastic materials," *Opt. Mater.* **29**(11), 1481–1490 (2007).
- P. Altschuh, W. Kunz, M. Bremerich, A. Reiter, M. Selzer, and B. Nestler, "Wicking in porous polymeric membranes: Determination of an effective capillary radius to predict the flow behavior in lateral flow assays," *Membranes* **12**(7), 638 (2022).
- A. Ley, P. Altschuh, V. Thom, M. Selzer, B. Nestler, and P. Vana, "Characterization of a macro porous polymer membrane at micron-scale by confocal-laser-scanning microscopy and 3D image analysis," *J. Membr. Sci.* **564**, 543–551 (2018).

- ²⁸C. A. Schneider, W. S. Rasband, and K. W. Eliceiri, "NIH image to ImageJ: 25 years of image analysis," *Nat. Methods* **9**(7), 671–675 (2012).
- ²⁹J. Hötzer, A. Reiter, H. Hierl, P. Steinmetz, M. Selzer, and B. Nestler, "The parallel multi-physics phase-field framework Pace3D," *J. Comput. Sci.* **26**, 1–12 (2018).
- ³⁰H. Darcy, *Les Fontaines Publiques De La Ville De Dijon: Exposition Et Application Des Principes à Suivre Des Formules à Employer Dans Les Questions De Distribution D'eau* (Victor Dalmont, Paris, 1856).
- ³¹W. Kunz, P. Altschuh, M. Bremerich, M. Selzer, and B. Nestler, "Establishing structure–property linkages for wicking time predictions in porous polymeric membranes using a data-driven approach," *Mater. Today Commun.* **35**, 106004 (2023).
- ³²P. Altschuh, *Skalenübergreifende Analyse Makroporöser Membranen Im Kontext Digitaler Zwillinge* (Karlsruher Institut für Technologie, 2020).
- ³³P. W. Hoffrogge, D. Schneider, F. Wankmüller, M. Meffert, D. Gerthsen, A. Weber, B. Nestler, and M. Wieler, "Performance estimation by multiphase-field simulations and transmission-line modeling of nickel coarsening in FIB-SEM reconstructed Ni-YSZ SOFC anodes I: Influence of wetting angle," *J. Power Sources* **570**, 233031 (2023).
- ³⁴M. R. Duncan, J. M. Lee, and M. P. Warchol, "Influence of surfactants upon protein/peptide adsorption to glass and polypropylene," *Int. J. Pharm.* **120**(2), 179–188 (1995).
- ³⁵P. Garidel, C. Hoffmann, and A. Blume, "A thermodynamic analysis of the binding interaction between polysorbate 20 and 80 with human serum albumins and immunoglobulins: A contribution to understand colloidal protein stabilisation," *Biophys. Chem.* **143**(1), 70–78 (2009).
- ³⁶W. Kunz, *Datengetriebene Analyse Der Strukturabhängigen Flüssigkeitsausbreitung in Porösen Membranen* (Karlsruher Institut für Technologie, 2024).
- ³⁷S. Peng, Q. Hu, S. Dultz, and M. Zhang, "Using X-ray computed tomography in pore structure characterization for a Berea sandstone: Resolution effect," *J. Hydrol.* **472–473**, 254–261 (2012).
- ³⁸T. Pak, I. B. Butler, S. Geiger, M. I. J. van Dijke, and K. S. Sorbie, "Droplet fragmentation: 3D imaging of a previously unidentified pore-scale process during multiphase flow in porous media," *Proc. Natl. Acad. Sci. U. S. A.* **112**(7), 1947–1952 (2015).
- ³⁹H. Tan, "Absorption of picoliter droplets by thin porous substrates," *AlChE J.* **63**(5), 1690–1703 (2017).
- ⁴⁰Y. Nagai, J. Eller, T. Hatanaka, S. Yamaguchi, S. Kato, A. Kato, F. Marone, H. Xu, and F. N. Büchi, "Improving water management in fuel cells through microporous layer modifications: Fast operando tomographic imaging of liquid water," *J. Power Sources* **435**, 226809 (2019).
- ⁴¹A. Kaestner, E. Lehmann, and M. Stampanoni, "Imaging and image processing in porous media research," *Adv. Water Resour.* **31**(9), 1174–1187 (2008).
- ⁴²R. K. Holman, M. J. Cima, S. A. Uhland, and E. Sachs, "Spreading and infiltration of inkjet-printed polymer solution droplets on a porous substrate," *J. Colloid Interface Sci.* **249**(2), 432–440 (2002).
- ⁴³Thermo Fisher Scientific, see <https://www.thermofisher.com/order/fluorescence-spectraviewer/#!/sharestate/7/6380ph8~21235p72~11001ph8/////~/40> for "Fluorescence SpectraViewer" (2025).
- ⁴⁴P. J. Yunker, T. Still, M. A. Lohr, and A. G. Yodh, "Suppression of the coffee-ring effect by shape-dependent capillary interactions," *Nature* **476**(7360), 308–311 (2011).
- ⁴⁵R. Dou and B. Derby, "Formation of coffee stains on porous surfaces," *Langmuir* **28**(12), 5331–5338 (2012).
- ⁴⁶R. D. Deegan, O. Bakajin, T. F. Dupont, G. Huber, S. R. Nagel, and T. A. Witten, "Capillary flow as the cause of ring stains from dried liquid drops," *Nature* **389**(6653), 827–829 (1997).
- ⁴⁷B. Markicевич, T. G. D'Onofrio, and H. K. Navaz, "On spread extent of sessile droplet into porous medium: Numerical solution and comparisons with experiments," *Phys. Fluids* **22**(1), 12103 (2010).
- ⁴⁸M. Hilpert and A. Ben-David, "Infiltration of liquid droplets into porous media: Effects of dynamic contact angle and contact angle hysteresis," *Int. J. Multiphase Flow* **35**(3), 205–218 (2009).
- ⁴⁹N. Alleborn and H. Raschler, "Spreading and sorption of droplets on layered porous substrates," *J. Colloid Interface Sci.* **280**(2), 449–464 (2004).
- ⁵⁰A. Lundberg, J. Ö. Örtengren, E. Alftan, and G. Ström, "Paper-ink interactions: Microscale droplet absorption into paper for inkjet printing," *Nord. Pulp Pap. Res. J.* **26**(1), 142–150 (2011).
- ⁵¹H. R. Charles-Williams, R. Wengeler, K. Flore, H. Feise, M. J. Hounslow, and A. D. Salman, "Granule nucleation and growth: Competing drop spreading and infiltration processes," *Powder Technol.* **206**(1), 63–71 (2011).
- ⁵²C. Grzelakowski, D. Ben Jazia, B. Lebeau, L. Vonna, D. Dupuis, and H. Haidara, "On the influence of pore structure on the free-imbibition of sessile drops into nanoporous substrates," *Langmuir* **25**(10), 5855–5860 (2009).
- ⁵³V. M. Starov, S. A. Zhdanov, S. R. Kosvintsev, V. D. Sobolev, and M. G. Velarde, "Spreading of liquid drops over porous substrates," *Adv. Colloid Interface Sci.* **104**(1), 123–158 (2003).
- ⁵⁴S. A. Zhdanov, V. M. Starov, V. D. Sobolev, and M. G. Velarde, "Spreading of aqueous SDS solutions over nitrocellulose membranes," *J. Colloid Interface Sci.* **264**(2), 481–489 (2003).
- ⁵⁵J. Cai and B. Yu, "A discussion of the effect of tortuosity on the capillary imbibition in porous media," *Transp. Porous Med.* **89**(2), 251–263 (2011).
- ⁵⁶K. Nakamura and K. Matsumoto, "Protein adsorption properties on a microfiltration membrane: A comparison between static and dynamic adsorption methods," *J. Membr. Sci.* **285**(1), 126–136 (2006).
- ⁵⁷Saiful, Z. Borneman, and M. Wessling, "Enzyme capturing and concentration with mixed matrix membrane adsorbers," *J. Membr. Sci.* **280**(1), 406–417 (2006).
- ⁵⁸K. Nakanishi, T. Sakiyama, and K. Imamura, "On the adsorption of proteins on solid surfaces, a common but very complicated phenomenon," *J. Biosci. Bioeng.* **91**(3), 233–244 (2001).
- ⁵⁹M. Martin and G. Guiochon, "Effects of high pressure in liquid chromatography," *J. Chromatogr. A* **1090**(1), 16–38 (2005).
- ⁶⁰F. Gritti and G. Guiochon, "Effect of the flow rate on the measurement of adsorption data by dynamic frontal analysis," *J. Chromatogr. A* **1069**(1), 31–42 (2005).
- ⁶¹A. E. Urusov, A. V. Zherdev, and B. B. Dzantiev, "Towards lateral flow quantitative assays: Detection approaches," *Biosensors* **9**(3), 89 (2019).